Beam physics studies for a high charge and high beam quality laser-plasma accelerator

Samuel Marini[1], Damien F. G. Minenna[1], Francesco Massimo[2], Laury Batista[1],
Vittorio Bencini[3], Antoine Chancé[1], Nicolas Chauvin[1], Steffen Doebert[3], John Farmer[4],
Edda Gschwendtner[3], Ioaquin Moulanier[2], Patric Muggli[4], Didier Uriot[1],
Brigitte Cros[2], and Phu Anh Phi Nghiem[1]

[1]*CEA, IRFU, DACM, Université Paris-Saclay, 91191 Gif-sur-Yvette, France*
[2]*LPGP, CNRS, Université Paris-Saclay, 91405 Orsay, France*
[3]*CERN, Geneva, Switzerland*
[4]*Max Planck Institute for Physics, Munich, Germany*

Electron acceleration by laser-plasma techniques is approaching maturity and is getting ready for the construction of particle accelerators with dedicated applications. We present a general methodology showing how beam physics studies can be used to achieve a specific parameter set in a laser-plasma accelerator. Laser systems, plasma targets, and magnetic component properties are designed to optimize the electron beam so as to achieve the required performances. Beam physics in its full 6D phase space is studied from electron injection to beam delivery to the end user, through the plasma acceleration stage and transport line. As each beam parameter can only be modified by specific electric/magnetic field configurations, it is crucial to assign from the beginning specific roles to given accelerator sections in obtaining given beam parameters. These beam physics considerations were successfully applied to the design of a plasma-based electron injector for the AWAKE Run2 experiment. Electron beam parameters were calculated using a global simulation, achieving simultaneously unprecedented high charge (100 pC) and high quality (micrometric beam emittance and size).

I. INTRODUCTION

Laser wakefield acceleration (LWFAs) is a promising concept for the development of compact electron sources. State-of-the-art experiments, supported by numerical simulations, have demonstrated that good-quality electron beams can be produced [1–5]. An intense laser pulse ($I \geq 10^{18}$ W cm^{-2}) focused into a plasma drives a plasma wave with large accelerating and focusing fields, which can be sustained over a cm scale, to deliver GeV electron beams. In this context, efforts are underway around the world to make possible the transition from acceleration experiments to accelerator facilities with practical applications and users [6,7]. A user facility must be able to deliver high-quality particle beams, where in addition to beam charge and energy, the evaluation of beam quality must also include energy spread, size, and divergence, involving 6D Twiss parameters and emittance [8–11].

Most promising studies of LWFAs are related to electron injectors, composed of a laser-plasma acceleration stage and a transport line. Electrons are generated by the ionization injection process in a mixed-gas plasma, accelerated to a 100–300 MeV energy range, and delivered to a transport line including magnetic elements. Beam physics studies have generally been conducted for the plasma or else for the transport line independently and have often been focused exclusively on given aspects of beam charge or beam quality. In [12–15], the transport line was optimized to reshape the input beam and to reduce its sliced energy spread for adapting it to free-electron-laser undulators. In [16–18], a transport line with a large energy acceptance and minimum sensitivity to pointing fluctuations was studied for injection into a second plasma acceleration stage. In [19], the focus was put on the control of the energy chirp by a dedicated transport line. In [20], it was pointed out that the laser beam quality and its focusing position in the plasma target are crucial to guarantee good electron beam quality. Optimizing the laser-plasma acceleration process was achieved by the authors of [5] by using extensive Bayesian methods to determine the best trade-off to obtain the best beam charge and energy spread, and in [21], random scans were performed to identify the solutions allowing to obtain targeted beam parameters.

For demanding applications such as free-electron-laser experiments, integrated studies were undertaken in [11], where the plasma target and the transport line are considered a whole set, and all the electron beam parameters are optimized simultaneously. For that study, the targeted beam charge was relatively modest (30 pC) and the transport lines considered were in a straight line. Another demanding application is to provide top-up injection into synchrotron light sources [22,23] where the targeted energy of 500–6000 MeV is higher than for currently studied LWFA injectors, making small energy spread easier to obtain at the plasma exit, while the requirement in energy spread at the transport line exit is so arduous that the use of an X-band rf cavity is needed.

To be competitive with conventional accelerators, a plasma-based injector should be capable of delivering to the end user a high charge (100 pC) and simultaneously high beam quality (micrometric normalized emittance, few % energy spread, suitable beam size and divergence) via a transport line that may need to include deviation dipoles. To attain this goal, in-depth analysis and understanding of the beam behavior and the means to handle its parameters are essential. We have developed and used a strategy of optimization centered on beam physics, relying on two main pillars: (i) studying beam physics in an integrated way, encompassing all the beam acceleration and beam transport sections, by attributing precise roles to each specific part in achieving well-identified beam parameters, in view of meeting the top-level requirements (i.e., beam performances asked by the end user). (ii) Performing massive optimizations by simulations, as for conventional accelerators, to define the optimum laser, plasma, and magnetic parameters, including their tolerances, capable of meeting the requirements on beam parameters formerly attributed.

The requirements on the electron beam parameters relate to the accelerator exit as well as along the accelerator. We have to keep in mind that specific beam parameters can only be tuned by appropriate electric or magnetic field configurations, which are exclusively present in given sections of the accelerator. For example, longitudinal electric fields affect beam energy, while transverse electric and magnetic fields affect beam focusing. In an LWFA, there are longitudinal and transverse electric fields in plasma cells that are not easy to precisely tune and magnetic fields in transport lines that can be precisely tuned. Consequently, given beam parameters can be modified only at precise locations of a LWFA, or in other words, if they are not set as desired in the most effective section, then enormous efforts will be needed to compensate for it in other sections. Even worse, certain parameters such as beam charge or emittance, can only be degraded in certain sections.

Acceleration and transport sections need to be studied in an integrated way, by assigning precise roles to these two sections. The role of an acceleration section is to produce and deliver a beam at the specified energy, and the specified charge and emittance with enough margin, knowing that these features will be deteriorated in the downstream transport line. In addition, according to [24–26], for limiting emittance growth in the transport line, energy spread must be limited to a few percent, and the Twiss parameter $\gamma_{x,y}$, limited to a few hundreds of m^{-1} by properly setting the exit plasma density profile. This gives an additional role to the plasma stage and a specific role to the plasma exit section, roles that are essential to ensure high beam quality at the accelerator exit. The role of a transport line is then to properly capture the beam exiting from the plasma and subsequently fine-tune it to obtain the sizes and divergences as required at its exit, all while minimizing emittance deterioration to fulfill any given requirements.

In this paper, we present an example of such beam physics considerations applied to the design of an electron injector for the AWAKE Run2 experiment [27,28]. This electron injector project is called EARLI (Electron Accelerator driven by a Reliable Laser wakefield for Industrial uses) [29]. In Sec. II, the EARLI project and the AWAKE experiment are briefly described, and the constraints and top-level requirements expected for the injector are listed. In Secs. III and IV, studies of the laser-plasma section and the beam transport section are presented, along with the beam requirements for each section as well as the strategies and optimizations applied to meet them. Results are then compared to requirements and the feasibility of their design is discussed. In Sec. V, the integrated beam physics study is assessed and its relevance for general LWFA studies is summarized.

II. EARLI PROJECT AND AWAKE RUN2 EXPERIMENT

An electron injector based on LWFA is designed for the AWAKE run2 experiment, offering an alternative to the conventional rf electron injector [30]. The current baseline is composed of an S-band rf gun, followed by X-band bunching and accelerating sections, and transport lines [31].

The AWAKE run2 experiment is seen as a first step toward future high-energy physics colliders. It consists in modulating the proton beam coming from the SPS (Super Proton Synchrotron) in a first 10-m-long rubidium plasma cell and to sending it into a second rubidium plasma cell where it drives a wakefield. Relativistic electrons coming from an external injector, such as EARLI, can be trapped and accelerated after injection in the second plasma, through the gap between the two rubidium plasma cells.

The EARLI injector includes two main components, as shown in Fig. 1: a laser-plasma acceleration (LPA) section (including a laser system and a plasma cell) and a transport line (TL). Based on the proton bunch repetition rate delivered by the CERN SPS, the EARLI injector is planned to operate with a repetition rate of 0.1 Hz. The AWAKE experiment configuration imposes the laser system and the
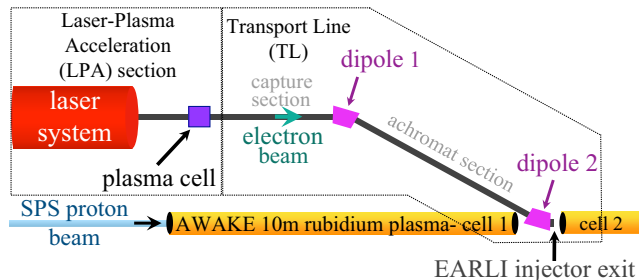
FIG. 1. Schematic layout of the EARLI laser-plasma based electron injector to be insert into the AWAKE environment. The electrons generated in the laser-plasma acceleration section (box on the left) are transported in the transport line (box on the right) up to the gap between the two rubidium plasma cells.

plasma cell to be installed on an axis parallel to the AWAKE main axis and the electron beam to be transported with a dogleg configuration to the ~1 m gap between the two rubidium plasma cells.

The EARLI project is proposed to meet the top-level requirements on beam parameters at the EARLI injector exit, which are listed in Table I. When considered individually, some of these requirements correspond to the current state of the art. However, achieving all these beam parameters together is very challenging and, up to now, has not been attempted, even at the plasma exit, while they have to be achieved at the user delivery point.

Implementing the EARLI injector would transform AWAKE into a full plasma accelerator with electrons generated and accelerated in plasma only, from both laser and proton drivers. In the long term, accelerators based on the EARLI design would be relevant for numerous applications such as light and particle sources, x-ray scanners [32], compact free-electron lasers (FEL) [33,34], short pulse probes, and research and development of sources for medical applications [35,36] using VHEE or flash therapy or initial elements of multistage LWFA collider facilities [37] for high-energy physics. Moreover, the EARLI project also includes many synergies with the EuPRAXIA [7] and PALLAS [21] projects toward LWFA user facilities. In EARLI injector, the required electron charge is particularly high, while relaxing only a little the other beam qualities.

With the results obtained in this article, it might be enough to reduce the charge by a collimator to get the beam charge and quality demanded in the other projects.

III. LASER-PLASMA ACCELERATION SECTION

The role of the laser-plasma acceleration section is to generate and inject electrons into the wakefield bubble, then accelerate them to the required energy and deliver the resulting beam to the transport line. To ensure the beam requirements in Table I can be met at the EARLI injector exit, those at the exit of the LPA section must be somewhat different [26]. They are listed in Table II. The charge must be higher than in Table I, while the emittance must be lower, in anticipation of their degradation in the downstream transport line. The constraints on beam sizes can be ignored, but two other constraints must be added: the energy spread should be limited to a few %, and the Twiss parameter $\gamma_{x,y}$ should be kept below a few hundred m^{-1}.

Note that obtaining such a high beam charge while maintaining such low energy spread and emittance induces significant challenges, which have never been targeted before for a laser-plasma acceleration section.

A. Strategy and optimizations

We consider LWFA based on ionization injection as it can provide a high electron charge and offer a good control on electron dynamics with a modest driving laser power. For the targeted electron beam energy, interactions between a 30 TW Ti:Sa laser pulse and a tailored density plasma are studied as illustrated in Fig. 2. After being injected by ionization [2,4,21,38–41] in a first zone containing a hydrogen-nitrogen gas mixture, electrons are accelerated in a second zone containing pure hydrogen gas and let to expand transversely in the third zone with hydrogen density lower by a factor of ~100 when compared to that of the second zone density, in order to decrease the Twiss parameter $\gamma_{x,y}$.

1. Laser setup

The laser pulse is assumed to be linearly polarized in the y direction and to exhibit a flattened Gaussian transverse intensity profile with $N = 6$, where N determines the

TABLE I. Top-level requirements on beam parameters at the EARLI injector exit.

Beam parameter	Top-level requirements
Charge (Q)	≥ 100 pC
Mean energy E	100–250 MeV
Normalized emittance $\epsilon_{x,y}$	≤ 2 μm rad
Beam size $\sigma_{x,y}$	6 μm
Twiss $\alpha_{x,y}$	0
Dispersion $D_{x,y}$	0
$D'_{x,y}$	0

TABLE II. Beam parameters expected at the exit of the laser-plasma acceleration (LPA) section.

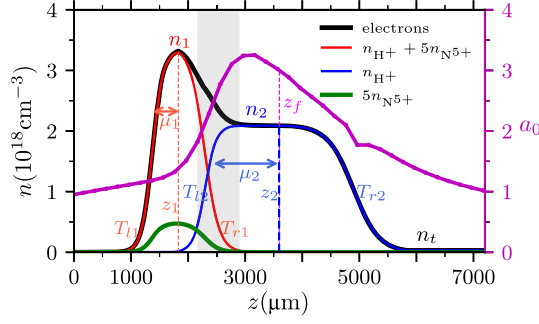| Beam parameter	Expected at the LPA exit
Charge Q	> 100 pC
Mean energy E	100–250 MeV
Energy spread σ_E/E	a few %
Normalized emittance $\epsilon_{x,y}$	< 2 μm rad
Twiss $\gamma_{x,y}$	a few hundreds m^{-1}

FIG. 2.   Longitudinal plasma density in a three-zone plasma cell. The first zone is a hydrogen-nitrogen plasma (red) where the nitrogen is represented by the green curve (enhanced 5×). In the second and third zones, there is a hydrogen plasma (blue curve), with the density in the third zone being 100 times lower than in the second zone. The total plasma density is represented by the black curve, and the gray region indicates where nitrogen ionization occurs. The magenta curve represents the normalized laser field amplitude (a_0).

flatness of the transverse profile [42,43], such that $N = 0$ corresponds to a Gaussian profile. At the focal plane, the envelope of the y component of the laser electric field in vacuum follows:

$$E_{\text{laser}} = a_0 \cdot E_0 \exp\left(\frac{-r^2}{(N+1)w_0^2} - \frac{t^2}{\tau_0^2}\right) \cdot \sum_{n=0}^{N} c_n' L_n^0\left(\frac{2r^2}{(N+1)w_0^2}\right), \quad (1)$$

with w_0 the waist at the focal position z_f, $\tau_0 = \tau_0'/\sqrt{2\ln 2}$ the laser field duration, τ_0' the FWHM laser intensity duration, $E_0 = m_e\omega_0 c/e$, the characteristic electric field amplitude, ω_0 the laser carrier angular frequency, c the speed of light in vacuum,

$$c_n' = \sum_{m=n}^{N} \frac{1}{2^m}\binom{m}{n}, \quad (2)$$

and L_n^0 the Laguerre polynomials. The peak amplitude of the normalized vector potential of the laser pulse field is $a_0 = \max[e|\mathbf{A}|/(m_e c^2)]$ with m_e and e the electron mass and charge and $|\mathbf{A}|$ the vector potential magnitude. Aiming to maintain the laser-plasma interaction weakly nonlinear, while exciting a wakefield with enough strength to accelerate a significant amount of charge to relativistic speed, we chose as starting values: $a_0 \sim 1.5$, $w_0 \sim 20$ μm, and $\tau_0 \sim 25$ fs. This corresponds to a laser power $P \sim 30$ TW, with a carrier wavelength $\lambda_0 = 0.8$ μm. These four parameters are to be finely optimized.

2. Plasma setup

The longitudinal plasma density in a three-zone plasma cell is depicted in Fig. 2. The plasma is assumed to be composed of two main plateaus of density n_1, n_2, and a tail

of much lower density n_t. The longitudinal density profile along z is expressed by [44]:

$$f(z) = n_1 s_1(z) + n_2 s_2(z)$$
$$+ \Theta(z - z_2)\Theta[n_t - n_2 s_2(z)][n_t - n_2 s_2(z)], \quad (3)$$

where Θ is the Heaviside step function, and the functions s_α, with $\alpha = 1$ or 2 are given by a double-normalized Fermi-Dirac function

$$s_\alpha(z) = \begin{cases} \frac{1+\exp(-\mu_\alpha/T_{l\alpha})}{1+\exp(-(\mu_\alpha+z-z_\alpha)/T_{l\alpha})}, & \text{if } z < z_\alpha, \\[2mm] \frac{1+\exp(-\mu_\alpha/T_{r\alpha})}{1+\exp(-(\mu_\alpha-z+z_\alpha)/T_{r\alpha})}, & \text{if } z \geq z_\alpha. \end{cases} \quad (4)$$

In Eq. (4), z_α is the central position of the plateau, μ_α its length, and $T_{l\alpha}$ (respectively, $T_{r\alpha}$) represents the density variation rate on the left (respectively, right) plateau side. Assuming the plasma is partially ionized by the laser pulse front ($I > 10^{14}$ W cm^{-2}), the density in the first zone is determined by the sum of electrons coming from hydrogen gas (1 per atom) and nitrogen gas (5 per atom, from the external L shell), while in the following zones, only hydrogen electrons are considered.

The plasma is thus described by 12 parameters that are to be optimized. Among them, the two main parameters, which must be estimated at the onset to be used as starting values for optimizations, are the density and the length of the second plateau, i.e., n_2 and μ_2. The scaling laws derived in [45] are used as a guide. In the blowout regime, a spherical accelerating bubble with radius $R = 2\sqrt{a_0}c/\omega_p$ is formed, where ω_p is the electron plasma frequency directly linked to the plasma density. Optimal acceleration conditions emerge when the laser waist size w_0 and the pulse length $c\tau_0$ are nearly equal to R, which means the density is in the range $n_2 \sim 3 \times 10^{17}$ cm^{-3} to 3×10^{18} cm^{-3}. The corresponding dephasing length $(2/3)(\omega^2/\omega_p^2)R$ results in $\mu_2 \sim 2500$ μm to 3500 μm, but in practice, μ_2 must be much lower to avoid laser depletion. With these parameters, in optimal acceleration and beam loading conditions, scaling laws in [2,45] indicate that hundreds of pC charge can be accelerated to hundreds of MeV energy. These are compatible with the required charge and energy of our case, but nothing is known about the corresponding beam quality in terms of emittance or energy spread.

3. Laser-plasma interaction and optimizations

The initially low intensity laser pulse entering the plasma in the first zone (corresponding to the region $z \lesssim 3000$ μm in Fig. 2) generates the plasma by ionization of hydrogen and outer-shell nitrogen electrons. By interacting with this underdense plasma, the laser is self-focused and self-compressed, resulting in rapid increase of its peak-field amplitude, which in turn enables the ionization of

inner-shell electrons in nitrogen when the laser intensity exceeds $I > 5 \times 10^{18}$ W cm^{-2} ($a_0 > 1.7$) [40].

By controlling the laser amplitude through the plasma density profile, the volume where ionization takes place can thus be determined. This volume plays a key role to determine the beam quality. In the second plasma zone where only hydrogen is present ($3000\,\mu\text{m} \lesssim z \lesssim 4500\,\mu\text{m}$), ionization is stopped, electrons are trapped in the wakefield bubble generated by the now more intense laser pulse and are strongly focused while accelerated to hundreds of MeV. In the third plasma zone ($z \gtrsim 4500\,\mu\text{m}$), characterized by significantly lower hydrogen density, focusing forces are moderate while acceleration is negligible. As a result, the bunch transverse size expands, reducing the Twiss parameter $\gamma_{x,y}$, as required.

Each of these three plasma zones must be thoroughly optimized, considering that they play specific roles on specific beam characteristics. Figure 3 illustrates how the electron beam's characteristics vary through these three plasma zones since it is generated. Careful examination of these figures is essential in our beam physics optimization procedure.

In the ionization zone where nitrogen is present (gray area), when discarding particles with energy below 25 MeV which will not be trapped and correctly accelerated later on, we observe that the beam charge increases almost linearly. In parallel, the emittance and energy spread also increase [Figs. 3(a) and 3(b)]. This zone should therefore be ended as soon as the charge increase begins to saturate. The charge finally obtained is fixed, and the emittance is mainly determined in this first plasma zone, as it will vary little downstream. This frontal competition between a high charge and a low emittance must be solved as best as possible by careful optimization of the laser power and focus position together with the plasma composition.

The transition between the ionization and the acceleration zone should also be optimized. Kirchen *et al.* [4] applied machine learning and identified a solution that features a small plasma density depression between the two plateaus, which is interesting for high electron energy ranges. However, we tested similar configurations and did not find in our case any advantage compared to a smooth transition.

The acceleration zone is dedicated to increase the electron beam energy, decreasing by the way the relative energy spread [Fig. 3(c)]. However, it also contributes to deteriorate a little the emittance [Fig. 3(b)], so its length and the plasma density are optimized so as to maximize the beam energy while keeping the emittance increase to a level compatible with the requirements. Besides this competition between high energy and low emittance, the competition between high charge and low energy spread must also be considered in this zone. Indeed, the final energy spread is determined by the variation of the accelerating (longitudinal) wakefield along the electron bunch, which can be
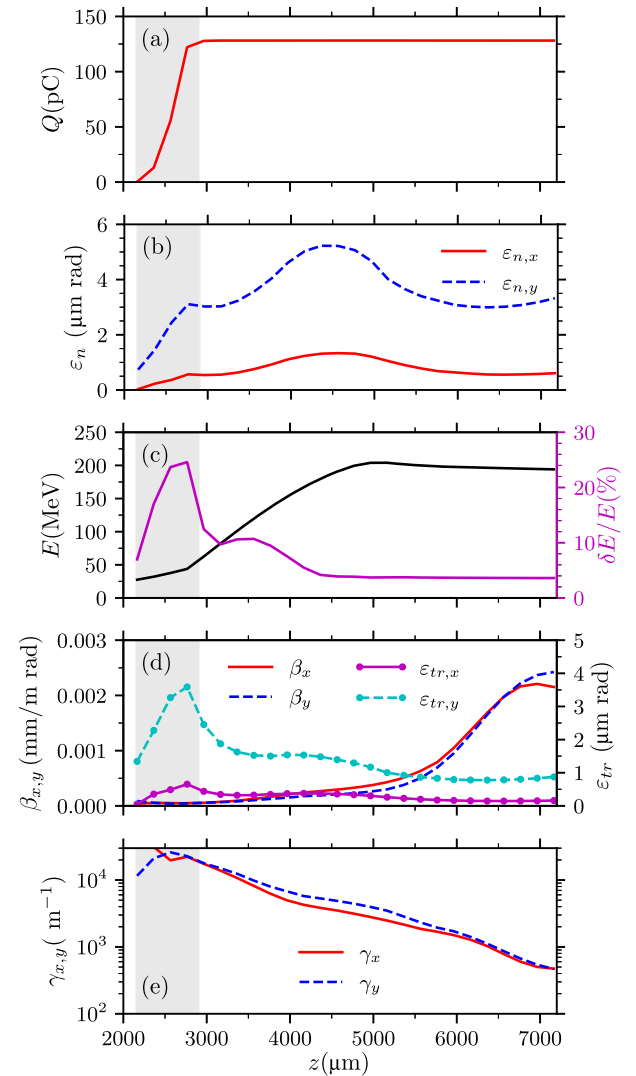

FIG. 3. Evolution in the plasma cell of (a) electron beam charge, (b) normalized emittance, (c) mean energy and its spread, (d) Twiss β and trace emittance, and (e) Twiss γ. The gray region indicates where nitrogen ionization occurs.

mitigated by a fine adjustment of beam loading [46], while a high charge generally leads to a larger bunch length induced by a longer generation duration in a longer ionization zone.

Regarding transverse electron beam parameters, namely its size and divergence, they are determined by the trace emittance and Twiss parameters (i.e., $\sigma_{x,y}^2 = \beta_{x,y}\varepsilon_{tr-x,y}$), which are governed by different mechanisms [Fig. 3(d)]. The trace emittance is larger in the plane of polarization of the laser pulse (y), due to the oscillation amplitude of the electric field vector **E**. On the contrary, the Twiss parameters $\alpha_{x,y}$, $\beta_{x,y}$, and $\gamma_{x,y}$ are similar in x and y, because they are entirely determined by focusing forces that have cylindrical symmetry since they are generated by ponderomotive forces that depend on the amplitude $|\mathbf{E}|^2$. Huge focusing forces in the second plasma zone lead to a tiny

beam transverse size and very large $\gamma_{x,y}$ in the $\sim 10^3 \, \text{m}^{-1}$ range [Fig. 3(e)], which should be damped to $\sim 10^2 \, \text{m}^{-1}$ with moderate focusing forces in the third plasma zone. The density and length of this downramp zone are optimized so as to decrease enough the Twiss γ, without deteriorating too much the emittance.

With these considerations, we can see that the three zones of the plasma, (i) the ionization and capture zone, (ii) the acceleration zone, and (iii) the downramp zone, play different roles in the achievement of the required beam parameters. They can then be studied and optimized most of the time separately, which will help to strongly shorten the simulation time compared to simulations with the whole plasma cell and also shorten any numerical optimizations. Alternating above beam physics optimizations and numerical methods could be recommended.

In total, 16 independent parameters should be optimized, 4 for characterizing the laser beam (a_0, w_0, τ_0 and focal position z_f) and 12 for the plasma density. The approach to obtain simultaneously all the expected beam parameters of Table II consists of a back-and-forth process between massive numerical optimizations and close scrutiny of beam characteristics along the tailored plasma.

First of all, published simulation results and scaling laws [2,4,7,46–48] were used to narrow down the initial parameter range used as an input for simulations. Following this, a first massive random scan with a few thousand Particle-in-Cell (PIC) simulations was performed for the plasma profile described in Fig. 2. The best beams were selected with the following order of priority: high charge, low

energy spread, and low emittance in *y*. Then parameters are further refined in the three separate plasma zones successively, according to the above beam physics considerations.

Different numerical methods have also been tried, including Bayesian and Genetic algorithms. While these methods yield interesting solutions, given our specific constrains, none have shown to be significantly better in obtaining the desired beam parameters.

B. Results- optimized beam parameters

Once a candidate solution was identified, small variations of variables around this solution were studied. This is useful from a triple point of view: (i) seeking for a better solution; (ii) understanding the effect of each input parameter; and (iii) estimating the sensitivity to errors, which is important for assessing the stability, the reproducibility, and the feasibility of a solution.

Figure 4 is an example of variations of the beam parameters versus variations of laser and plasma parameters around the selected candidate solution, in which the input parameters (also used to build Figs. 2 and 3) are described in Table III and outputs in Table IV. Overall, this figure suggests that such a solution is at a (local) minimum for the emittance and/or the energy spread, stressing that these two criteria, both directly related to beam quality, were the hardest to obtain as they call for a fine compromise. Comparatively, the beam charge and energy seem not to reach any optimum, which is not worrying in our case, as the requirements on those criteria are looser. This also suggests that other solutions do exist, with other values of
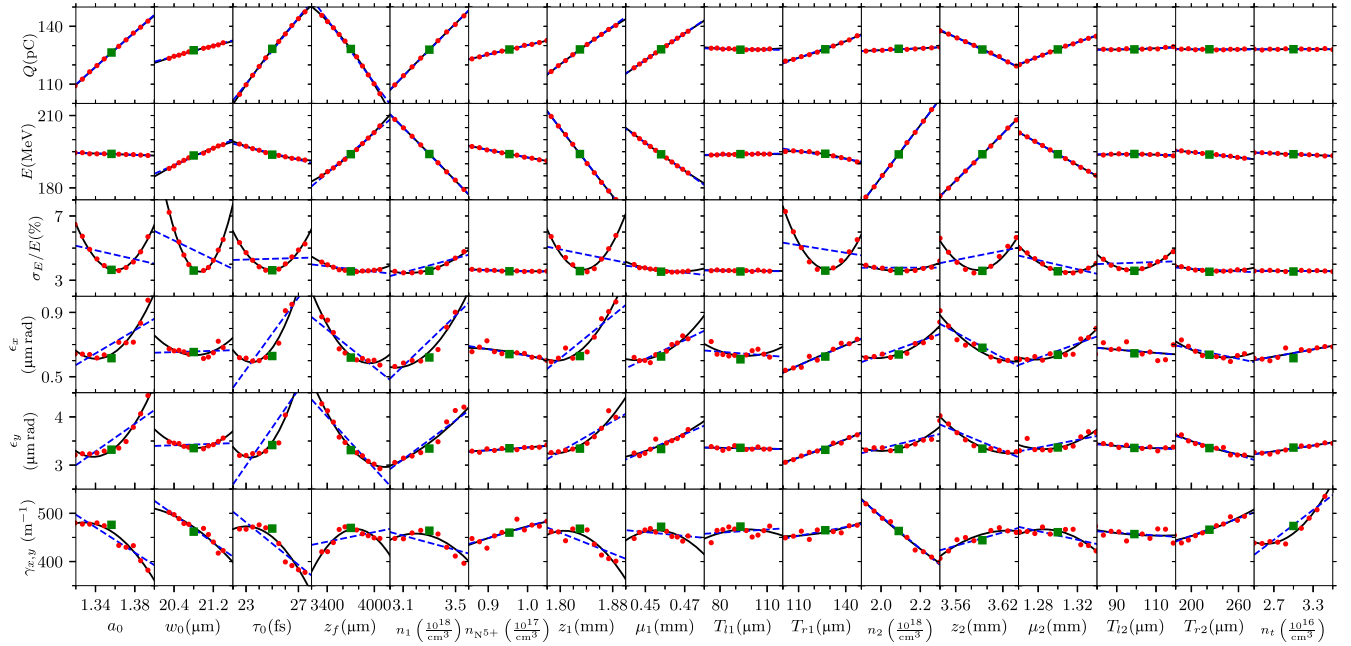

FIG. 4. Output beam parameter variations (rows) versus input laser and plasma parameter changes (columns). Red points show PIC simulation results with FBPIC, around a candidate solution (green point) described in Table III. Dotted and solid lines represent linear and quadratic fits, respectively.

TABLE III.   Laser and plasma parameters used to obtain the candidate solution from the LPA simulation.

Laser parameters		Plasma parameters	
a_0	1.36	z_1	1830 μm
w_0	20.9 μm	z_2	3594 μm
τ_0 (field)	25 fs	μ_1	458 μm
z_f	3700 μm	μ_2	1300 μm
		T_{r1}	93 μm
		T_{l1}	127 μm
		T_{r2}	99 μm
		T_{l2}	223 μm
		n_1	3.300×10^{18} cm^{-3}
		n_2	2.090×10^{18} cm^{-3}
		$n_{N^{5+}}$	0.953×10^{17} cm^{-3}
		n_t	3.000×10^{16} cm^{-3}

the couple charge/energy and as good local minima for the couple emittance/energy spread. The adjustment of Twiss $\gamma_{x,y}$ is made only at the end, consisting in decreasing it as far as possible with the third plateau parameters, without deteriorating the other parameters.

Numerical configuration for the simulations performed with FBPIC and SMILEI particle-in-cell (PIC) codes are detailed in the Appendix. Building on the approach described in previous sections, numerical optimizations were performed. The obtained optimal laser pulse and plasma characteristics described in Table III lead to the electron beam at the LPA exit, outlined in Table IV, that meets the expectations listed in Table II. This is especially true regarding the high charge of 128 pC, along with a μm rad range emittance and a low energy spread. Note that the obtained normalized emittance $0.6 \times 3.2 = 1.92$ (μm rad)^2) corresponds to a 4D normalized emittance that is twice better than the top-level requirement of $2 \times 2 = 4$ (μm rad)^2. The Twiss $\gamma_{x,y}$ is in the range of a few thousand m^{-1} at the second plasma zone exit. It has been decreased to a few hundred as expected thanks to careful optimization in the third plasma zone.

TABLE IV.   Beam parameters obtained at the LPA exit. To be compared to expected values in Table II.

Beam parameter	Obtained at the LPA exit
Charge (Q)	128 pC
Mean energy E	194 MeV
Energy spread (std)	3.60%
Energy spread (mad)	1.71%
Normalized emittance ϵ_x	0.6 μm rad
Normalized emittance ϵ_y	3.2 μm rad
Twiss γ_x	467 m^{-1}
Twiss γ_y	466 m^{-1}
Beam size (1-rms) σ_x	1.89 μm
Beam size (1-rms) σ_y	4.71 μm
Beam size (1-rms) σ_z	2.5 μm

An overview of this electron beam is presented in Fig. 5, where the beam 6D phase space is shown. These figures show the beam distribution's remarkable compactness, which is indicative of the beam's good quality, beyond just numerical values.

The phase space representing the energy along the beam [panel (c)] is particularly meaningful, from a double point of view: (i) The average thickness of this distribution (also called slice energy spread) is caused by the initial ionization process and may be improved only in the first plasma zone. (ii) The average shape, i.e., slope or undulation, of this distribution is caused by the longitudinal electric field seen by the beam at different positions along its length during the acceleration process. This average shape being horizontal and flat over almost the whole beam length suggests that the beam loading effect [49] perfectly compensates for the wakefield variation, except at the two extremities. No major further improvement can be expected in this aspect. Though meeting the expectations of Table II, the output beam of this section still needs to prove that it allows to meet the top-level requirements of Table I after transport by the downstream transport line.

C. Discussions

The presented results exhibit beam parameters that meet all the expectations of Table II. Its feasibility is discussed in the following. Details on simulations with two PIC codes, FBPIC and SMILEI, are given in the Appendix. Number of particles, number of cells, and box sizes were chosen to
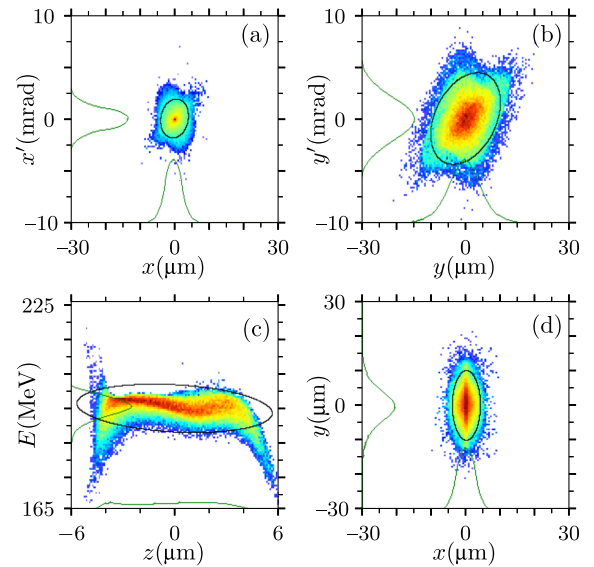

FIG. 5.   6D beam phase space at the LPA exit as described in Table IV. (a) horizontal phase space $x - x'$; (b) vertical phase space $y - y'$; (c) longitudinal phase space $z - E$; (d) transverse plane $x - y$. Black ellipses represent the 5-RMS emittance, and green curves are the 1D projections on the axes. The superscript prime denotes variations of coordinates along the transport lone. These results were obtained using the FBPIC PIC code.

ensure convergence of the simulated results, and the successful benchmark between the two distinct codes, each employing completely different approaches, attests the results to a certain degree of realism. Furthermore, these results have not only been obtained by massive optimization methods but also by understanding of the specific physical phenomena involved at each injection-acceleration stage and then by finely adjusting them. This is a proof of their physical realism, and in addition suggests that they can be reached in real life by adjusting the appropriate physical parameters, provided the latter can be measured and controlled. The robustness of the solution, i.e., its sensitivity to errors, can then be examined. Figure 4 gives a rough idea about variations in the output beam parameters caused by laser pulse or plasma variations. This shows how precisely these experimental parameters must be controlled. However, let us stress that none of these parameters must be achieved specifically at the indicated values. Variations in one parameter value can be compensated by adjustments in another to maintain the desired beam properties.

In general, it is clear that there is a conflict between achieving a high charge on one side and a low emittance, low energy dispersion on the other. However, the present studies show that there are still enough margins on both sides, meaning that other solutions do exist with less charge and better beam quality or vice versa. For example, using a plasma density profile quite different from the smooth profile in Fig. 2, presenting perfectly flat plateaus linked by straight slopes, i.e., a piecewise linear function, an alternative solution can be found, with less charge and better beam quality: $Q = 117$ pC, $E = 189$ MeV, $\sigma_E/E = 2.6\%$, $\epsilon_y = 3.2$ μm rad, $\epsilon_x = 0.54$ μm rad, Twiss $\gamma_y = 264\,\mathrm{m}^{-1}$, and $\gamma_x = 211\,\mathrm{m}^{-1}$ to be compared to parameters obtained previously in Table IV. As discussed in the following, this LPA alternative solution can also be transported in the same downstream transport line, yielding electron bunches that meet all top-level requirements.

IV. ELECTRON BEAM TRANSPORT LINE

The role of the transport line is to properly capture the electron beam coming from the plasma and to transport it to the end user, here the AWAKE experiment so that all the beam requirements are met there. This includes two major tasks: (i) minimize as much as possible the emittance growth despite the significant energy spread, which is made possible thanks to the low Twiss parameter $\gamma_{x,y}$ of the order of a few hundred m^{-1} at the plasma exit [see Eq. (5) and (6) hereafter], and the still available small margin with requirements and (ii) realize the required Twiss parameters $\alpha_{x,y}$ and $\beta_{x,y}$ at the transport line exit in order to match the beam to the downstream plasma focusing channel of the AWAKE experiment.

These two requirements are fulfilled through the optimization strategy developed in the following. We will also highlight all the specific properties of this strategy to show it is useful for the design of any transport lines within the plasma-based accelerator context.

A. Strategies and optimizations for transport lines

The generation and acceleration of electrons on an axis parallel to the AWAKE main axis impose a double-dipole dogleg configuration for the injection line (Fig. 1). Due to the limited available space at the injection point, approximately 1 m, the transport line should end at the second dipole, with no or very few other elements downstream. In any case, the number of quadrupoles to be used should be adequately determined. Not enough will not allow to achieve all the beam requirements, and too many will lead to false needs of very strong gradients due to contradictory actions between quadrupoles. As eight transverse beam parameters ($\alpha_{x,y}$, $\beta_{x,y}$, dispersion function $D_{x,y}$, and derivative $D'_{x,y}$) must be tuned, at least eight quadrupoles are needed. The starting configuration is a minimum configuration and includes a capture section with three quadrupoles and an achromat section with five quadrupoles (see Fig. 1). All the magnets are regular electromagnets, quadrupoles are 150 mm long, and dipoles are 750 mm long with a field of 0.2 T.

Optimizations in TraceWin [50] envelope mode were first carried out to evaluate the linear behavior of that minimum configuration. It was found to be flexible enough for a required beam size at the exit of the order of a few dozen of μm. Here, a few μm beam size is required so that specific drift lengths are needed, and this minimum configuration does not provide enough flexibility for tuning the beam size. Quadrupoles that allow fine-tuning of the beam size at exit are contained in the achromat section but are also bound to the rules of the achromat and, therefore, partially lose their tuning capacity. The solution consists in adding a fourth quadrupole in the capture section, allowing to achieve the beam size and divergence in the two transverse planes as desired at the achromat entrance. With the $4 + 5$ quadrupoles configuration, all the requirements can be fully met in envelope mode simulations. For beam sizes very different in x and y, as here for the beam coming from an LPA with ionization injection, it is preferable to rotate the beam so that the plane with greater beam size aligns with the dispersion function plane (i.e., x direction). This orientation prioritizes focusing on this plane to minimize dispersion function growth in the achromat. So, please note that here we rotated the beam coming from the LPA by 90° to align its axis of greatest size with the x direction. On the real machine, it should be done by providing a beam with a bigger emittance in the x direction with a laser polarized in x from the start.

The strongest issues appear, as expected, in TraceWin multiparticle simulations, due to the very strong nonlinearities induced by the beam emittance and energy spread that are several orders of magnitude higher than in conventional accelerators. These issues are made worse

when a strong focusing gradient must be applied to obtain smaller, micrometric beam sizes at the end. According to [26], the emittance growth after crossing a free drift of length l is given by

$$\epsilon_{\rm ph}^2 - \epsilon_{\rm ph0}^2 = \epsilon_{\rm tr\,0}^2 p_0^2 \left(\frac{\sigma_p}{p_0}\right)^2 l \gamma_0 (l \gamma_0 - 2\alpha_0), \qquad (5)$$

and after crossing a thin lens of integrated normalized gradient k is given by

$$\epsilon_{\rm tr}^2 - \epsilon_{\rm tr\,0}^2 = \epsilon_{\rm tr\,0}^2 \beta_0^2 k^2 \left(\frac{\sigma_p}{p_0}\right)^2, \qquad (6)$$

where $\epsilon_{\rm ph}$ and $\epsilon_{\rm tr}$ stand for phase and trace emittances, α, β, and γ for Twiss parameters, σ_p/p_0 for rms relative energy dispersion, and subscript 0 for parameters at element entrance. Note that minimizing β_0 amounts to minimizing γ_0 in the drift preceding the lens.

Typically, when using the tuning solution found with envelope simulations for multiparticle simulations, the beam emittance and sizes are multiplied by factors of more than 30, and, the beam projected in the transverse phase spaces (x, x') and (y, y') takes the shape of a butterfly or an hourglass. In these conditions, the quantities, such as ϵ and σ, are very poor descriptions of the beam.

Efforts were thus concentrated on the damping of the many nonlinearities. For that, the figure of merit to be considered is beam emittance.

The first idea coming to mind is to use sextupoles. They can compensate for the focusing defects induced by quadrupoles due to energy differences between particles. They are the most effective when located (i) within the quadrupoles or closest to them, in order to correct the aberrations at their source, and (ii) where the dispersion function is the highest, i.e., where particles of higher energies are farther from the central axis and thus can be more focused by sextupoles. Consequently, we used four sextupoles placed within the four quadrupoles in the achromat (the dispersion function is close to zero at the achromat central quadrupole). Fine numerical optimizations lead to emittances at exit $\epsilon_x \sim 100$ μm rad, $\epsilon_y \sim 4$ μm rad (starting from 3.2 and 0.6 μm rad at input). Higher-order magnets, such as octupoles, were also tested but the additional improvement was found to be marginal.

Further efforts were then dedicated to minimize the local emittance growths reaching 20 μm rad in the capture section, and even 3000 μm rad in the achromat, due to the nonzero dispersion function.

To reduce the emittance growth in the capture section, we applied the recommendations expressed in [26] for the EuPRAXIA project [7]. First, the Twiss $\gamma_{x,y}$ parameter upon exiting the LPA is required to remain of the order of a few hundreds. As shown in Table IV, this criterion is already met for our candidate solution, with $\gamma_{x,y} \approx 470$ m^{-1}.

Second, very strong and short quadrupoles were used very close to the LPA exit, in order to further decrease $\gamma_{x,y}$ as quickly as possible. Such quadrupoles can only be made of permanent magnets. The use of four permanent magnet quadrupoles allows to reduce the emittance in the capture section to 10 μm rad while focusing the beam down to $\sigma_{x,y} \sim 100$ μm at the achromat entrance.

Let us specify that the first quadrupole is positioned at 50 mm from the plasma exit. The pertinence of this short distance can be also understood via considerations of the so-called chromatic length $L_{\rm ch}$ introduced in [15]. It is the drift length over which the phase emittance increases by a factor of $\sqrt{2}$ when starting from a beam waist (i.e., $\alpha_{x,y} = 0$). In Ref. [26], it is expressed as $L_{\rm ch} \approx 1/(\gamma_{x,y}\sigma_E/E)$, where we can see that reducing $\gamma_{x,y}$ leads to increasing $L_{\rm ch}$. For the present case, $L_{\rm ch} = 60$ mm; then, it is bigger than 50 mm as expected. Anyway, $L_{\rm ch}$ can only play an indicative role here, because we do not have a beam waist at the plasma exit, where $\alpha_x = -0.148$ and $\alpha_y = -0.366$.

Note that when $\gamma_{x,y}$ is further reduced to ~ 200 m^{-1} as in the alternative solution presented earlier (Sec. III C), the emittance growth in the capture section is practically canceled. This suggests that, in case there is no geometric constraint, a straight transport line with four permanent magnet quadrupoles as here, is perfect in all aspects to connect two plasma acceleration stages. In less than 2 m, it also provides enough space to extract the laser beam and to implement electron beam diagnostics. As specified in [26], to avoid strong emittance growth, it is necessary to tune the plasma density at the exit of the first plasma so as to decrease the $\gamma_{x,y}$ to a few hundred m^{-1}, and that at the entrance of the second plasma so as to relax the coupling condition on $\beta_{x,y}$ by 1 to 2 orders of magnitude with non-null $\alpha_{x,y}$.

To reduce the emittance growth in the achromat, shorter dipoles were used and quadrupoles were placed closer to them to reduce the dispersion growth, while quadrupole positions were adjusted so as to minimize their strengths. With a ~ 1 T field dipole, which can still be an electromagnet, the dispersion function in x direction goes down to 200 mm (from 350 mm when using longer dipoles with 0.2T field) and the maximum emittance in the achromat goes down to ~ 1500 μm rad. With all these changes in the transport line magnetic structure, the exit emittances are $\epsilon_x = 52$ μm rad and $\epsilon_y = 2$ μm rad.

An additional method to damp nonlinearities is to remove particles with the highest off-energy, by means of a collimator located at the first quadrupole of the achromat section, close to the region where both the x dispersion function D_x and the correlation between the horizontal position and energy are maximum. A second collimator at the second quadrupole of the achromat section was used to remove particles far from the center in the transverse plane. Adjusting the collimator size to keep a

minimum charge of a 100 pC, starting from 128 pC at the exit of the LPA, leads to an improved beam emittance $\epsilon_x = 4.5$, $\epsilon_y = 0.8$ μm rad, and rms size of $\sigma_x = 99$ and $\sigma_y = 76$ μm at the transport line exit. To reduce the beam size at the transport line exit to a few μm as required, two additional small permanent-magnet quadrupoles downstream the achromat were added. Note that this symmetry between the beam line entrance and exit is necessary for limiting emittance growth, particularly when the incoming or outgoing beams have rms sizes on the order of a few μm.

B. Results

All numerical simulations and optimizations for the transport line have been performed with the TraceWin code [50]. The beam obtained at the transport line exit has parameters very close to requirements (Table V). Although the emittance in the x direction does not meet the constraints, the transverse 4D emittance is smaller than required. Indeed, the 4D emittance $4 \times 0.7 = 2.9$ (μm rad)^2 is below the required 4D emittance of $2 \times 2 = 4$ (μm rad)^2. A footprint of this electron beam is presented in Fig. 6, where typical 2D projections of the beam 6D phase space are shown. Note that the slice energy spread in Fig. 6(c) is much smaller than in Fig. 5(c), due to the chromatic effects introduced by the dipoles, stretching significantly the longitudinal space.

The total length of the transport line is around 8m. Its layout and the 1-rms beam envelopes are shown in Fig. 7. The Twiss parameter $\beta_{x,y}$ and dispersion functions are shown in Fig. 8. In the capture section (before the first dipole), there would be enough room to implement a laser beam extraction device and diagnostics. In the achromat (between the two dipoles), there would be enough room to implement diagnostics. The space taken by the transport line on the AWAKE main axis is less than 0.5 m.

The magnetic components required include two dipoles with the magnetic field of 1.167 T field (15° bend); in the capture section, four permanent quadrupole magnets with

TABLE V. Beam parameters obtained at the transport line exit. To be compared with the top-level requirements in Table I.

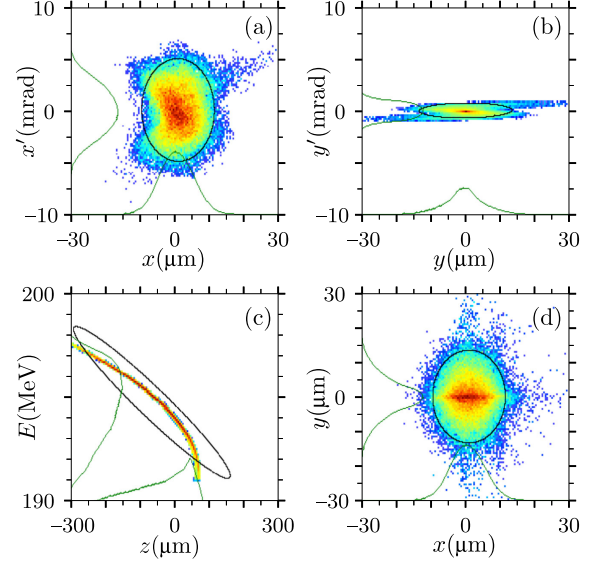| Beam parameter	Obtained at the transport line exit
Charge Q	≥ 100 pC
Mean energy E	194 MeV
Normalized emittance ϵ_x	≤ 4 μm rad
Normalized emittance ϵ_y	≤ 0.7 μm rad
Beam size σ_x	4.8 μm
Beam size σ_y	6.0 μm
Beam size σ_z	67.7 μm
Twiss α_x	0.006
Twiss α_y	-0.05
Dispersion $D_{x,y}$	0
$D'_{x,y}$	0

FIG. 6. 6D beam phase space at the LPA exit as described in Table IV. (a) horizontal phase space $x - x'$; (b) vertical phase space $y - y'$; (c) longitudinal phase space $z - E$; (d) transverse plane $x - y$. Black ellipses represent the 5-RMS emittance, and green curves are the 1D projections on the axes. The superscript prime denotes variations of coordinates along the transport lone. These results were obtained with the TraceWin code.

gradients ranging from 40 to 300 T/m; in the achromat section, five electromagnetic quadrupoles with gradients from 5 to 10 T/m, with sextupole components ranging from 20 to 50 T/m^2; and two additional permanent quadrupole magnets at the end of the line with gradients in the range of 150–350 T/m. For an injector intended to a research experiment that would need a high degree of versatility, the permanent magnets would be recommended to be variable, following the design established in [51]. Correctors and diagnostics are also needed. These devices remain to be studied in detail, following the general strategy
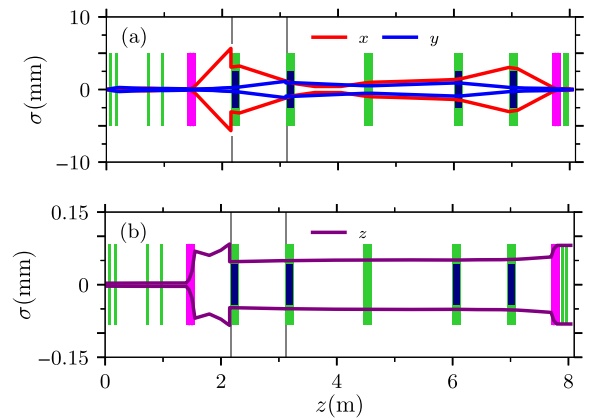

FIG. 7. Beam envelopes (1-rms) along the transport line, in the transverse (a) and in the longitudinal direction (b). Dipoles are in purple, quadrupoles in green, sextupoles (inside the quadrupoles) in black, and collimators in gray.
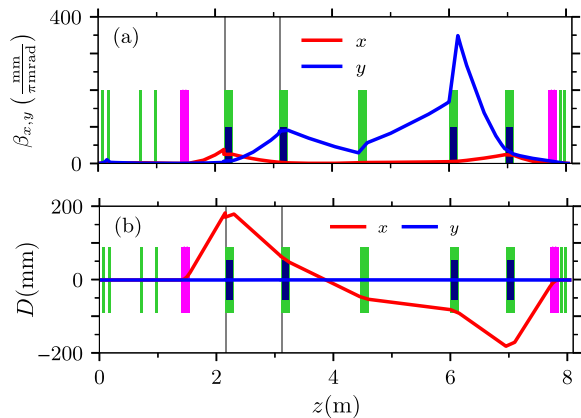
FIG. 8. Twiss parameter $\beta_{x,y}$ (a) and dispersion function D along the transport line (b). Dipoles are in purple, quadrupoles in green, sextupoles (inside the quadrupoles) in black, and collimators in gray.

defined in [29], where tolerances, correctors, and diagnostics are tightly related. According to that, we can estimate the needed correction configuration. For the achromat, we know that, if the 0.1 mm (1-rms) alignment error of electromagnet quadrupoles is tolerable, and if there is one corrector in x and y in each quadrupole or very nearby, then the requested corrector strength is fully feasible. This assumes there is one beam position measurement per quadrupole, located as far as possible in the drift next to the quadrupoles. The same reasoning can be applied to permanent magnet quadrupoles. We will see that, due to their very strong gradient, the needed corrector will also be very strong, especially for those at the end of the line where μm beam size must be delivered. Motorized positioning of permanent magnets is preferable. Emittance measurements are also needed in the capture sections and in the achromat. Two collimators in x and y, located at the entrance of the first and the second achromat quadrupole, should be considered.

C. Discussions

Detailed studies of error tolerances remain to be performed. However, the numerical simulations during the many optimizations carried out so far indicate that, except for the micrometric beam size requirements at output, for all other requirements, sensitivity to errors in the transport line seems to be manageable. The main reason is that, for the achromat, smooth, weak focusing was particularly sought. We observed that the same set of sextupoles can often be suitable for slightly different sets of quadrupoles. For each given situation, quadrupole or sextupole gradients should be likely properly compensated for, but a variety of different sets of gradients are suitable. The permanent magnets in the capture section need to be strong in order to decrease the Twiss parameter $\gamma_{x,y}$ as early as possible, but there is no need to set them at precise values, as they can compensate each other to give the same result. The

statement for the two strong permanent magnets downstream the achromat is a bit different, as they must be adjusted precisely according to the final beam size, typically on the order of a few micrometers. The best proof of this configuration's high flexibility is that, even in the case of a very different input beam coming from the LPA, as for the two alternative solutions presented in the previous section, a rapid retuning is enough to recover the beam meeting all the top-level requirements. For example, it is possible to transport the alternative LPA beam introduced earlier, obtained from a piecewise linear plasma function (Sec. III C).

The above comments suggest a real-life tuning easiness. With a regular sensitivity to errors as in conventional accelerators, and optimizations based on beam emittance and size measurements that should be available online, the tuning of the transport line would not face particular issues (except for the need of a few μm beam size at the exit). This is at least valid for static tuning. For dynamic tuning, all depends on the jitter amplitudes.

So far, nothing has been done to manage the final longitudinal beam size σ_z, so note that there is no real flexibility to vary it, contrary to the transverse beam sizes. With the present transport line configuration, σ_z varies inversely with the energy spread, which can be in a certain degree controlled by the collimator located at the first quadrupole. As a consequence, smaller σ_z can be obtained only with less charge and better transverse parameters; inversely, larger σ_z can be obtained with higher charge and not as good transverse parameters.

V. CONCLUSIONS

With the help of consistent strategies based on beam physics and by means of substantial numerical optimizations, an integrated design of the EARLI accelerator has been achieved, with exit beam parameters very close to the top-level requirements. This was only possible thanks to the assignment, from the beginning, of specific roles to each section regarding obtaining specific beam parameters best suited to its electric/magnetic field configuration while preparing the beam parameters according to the needs of the next section.

Detailed studies of sensitivity to errors remain to be performed, but the many numerical optimizations seem to show a smooth behavior versus technical features. Furthermore, they highlight the existence of not only one solution, but a set of solutions, with more or less charge with better or less good beam quality, which can be found by given sets of input parameters. Overall, the most important outcome of these studies is that the desired charge and beam quality can be achieved when enough technical features can be controlled, namely: the laser beam power, waist and duration, the three plasma density plateaus and the transitions between them, the four permanent-magnet quadrupoles of the capture section, the five electromagnet quadrupoles of the achromat section,

and the last two permanent-magnet quadrupoles. This work opens the way to laser-plasma-based accelerators with simultaneously high charge and high beam quality.

ACKNOWLEDGMENTS

APPENDIX: NUMERICAL SETTINGS IN FBPIC AND SMILEI CODES

Numerical simulations for the laser-plasma setups were performed using the FBPIC particle-in-cell (PIC) code [42]. In order to ensure the robustness of the results, comparisons on a typical solution with the SMILEI PIC code [52] have been performed. To benchmark the description of the relevant laser-plasma interaction, different models and numerical techniques have been selected from those available in the two codes.

In our FBPIC PIC simulations, the laser-plasma interaction is described in a cylindrical geometry with azimuthal mode decomposition [53], where two azimuthal modes $m = 0, 1$ are used. The FBPIC simulations rest on a moving window in the boosted frame [54] with Lorentz factor $\gamma_{boost} = 4.5$ and dimensions of 70×150 μm, discretized with 3500×450 cells in the longitudinal and radial directions, respectively. The time step is 66.7 as. The plasma is initialized with cold H^+ and N^{5+} ions in the first zone and cold H^+ in the second and third zones. Hydrogen (reciprocally, nitrogen) is represented by $2 \times 4 \times 1$ (reciprocally, $4 \times 4 \times 2$) macroparticles in the (r, θ, z) directions. Convergence tests were performed with lower resolutions. Ionization in FBPIC is handled using an algorithm based on the direct current, Ammosov-Delone-Krainov (DC ADK) ionization rate [55].

In our SMILEI PIC simulations, the laser-plasma interaction is also described in a cylindrical geometry but with only one azimuthal mode [56]. Moreover, there, the laser pulse is described by an envelope model [57,58], where the envelope equation describing the laser envelope evolution is solved through an explicit solver that presents reduced numerical dispersion, as described in [57]. SMILEI PIC simulations use a moving window discretized with 3584×448 cells of size $\Delta x = 0.019$ μm, $\Delta r = 0.33$ μm in the longitudinal and radial direction, respectively, and a time step $\Delta t = 0.98 \Delta x / c = 62.1$ as. The physical parameters of the laser pulse and of the plasma are the same as in the FBPIC simulation. Hydrogen and nitrogen are represented by $4 \times 2 \times 1$ macroparticles in the longitudinal, radial directions and the azimuthal angle. The ionization is modeled as a function of the laser envelope through an averaged tunnel ionization model [59]. To considerably
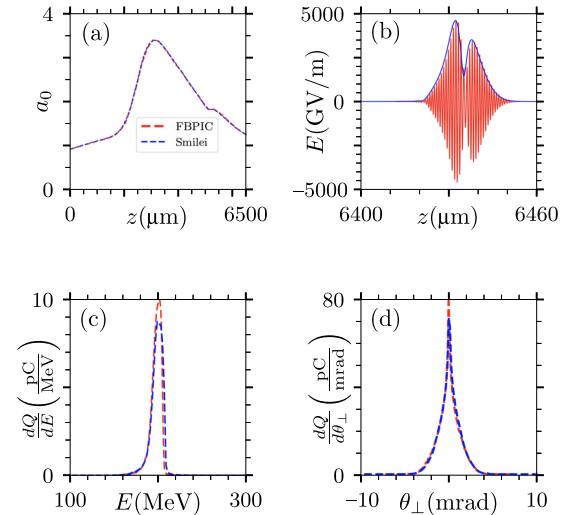
FIG. 9. (a) Evolution of the laser normalized transverse electric field. (b) Snapshot of the transverse electric field (the absolute value of its envelope for the SMILEI simulation) on the laser propagation axis. (c) Electron beam energy spectrum after 6400 μm of laser propagation. (d) Angular spectra at the same laser propagation distance. These figures were built using both FBPIC and SMILEI PIC codes.

reduce the effects of numerical Cherenkov radiation, a B-TIS3 interpolation scheme is used [60].

Panel (a) of Fig. 9 displays the evolution of the laser-normalized peak transverse electric field along the plasma (Fig. 2) obtained with both PIC codes, and an excellent agreement between them can be inferred. Panel (b) shows a snapshot of the transverse electric field E_y (the absolute value of its envelope for the SMILEI simulation) on the laser pulse propagation axis after 6400 μm of propagation. The envelope model used in SMILEI successfully describes the deformation of the laser pulse envelope after propagation in the plasma. Panel (c) displays the electron beam energy spectrum obtained with FBPIC and SMILEI after 6400 μm of laser pulse propagation. The difference in total charge is only 2.4%, the peak energy is essentially the same, as well as the energy spread spectrum. Panel (d) shows the comparison of the angular spectra at the same propagation distance in the perpendicular direction ($\theta_\perp$). The similarity between the results obtained with the two codes emphasizes the robustness and coherence of the two approaches in modeling the system.

[1] E. Esarey, C. B. Schroeder, and W. P. Leemans, Physics of laser-driven plasma-based electron accelerators, Rev. Mod. Phys. **81,** 1229 (2009).

[2] J. P. Couperus, R. Pausch, A. Köhler, O. Zarini, J. M. Krämer, M. Garten, A. Huebl, R. Gebhardt, U. Helbig, S. Bock *et al.*, Demonstration of a beam loaded nano-coulomb-class laser wakefield accelerator, Nat. Commun. **8** (2017).

[3] A. Gonsalves, K. Nakamura, J. Daniels, C. Benedetti, C. Pieronek, T. de Raadt, S. Steinke, J. Bin, S. Bulanov, J. van Tilborg et al., Petawatt laser guiding and electron beam acceleration to 8 GeV in a laser-heated capillary discharge waveguide, Phys. Rev. Lett. 122, 084801 (2019).

[4] M. Kirchen, S. Jalas, P. Messner, P. Winkler, T. Eichner, L. Hübner, T. Hülsenbusch, L. Jeppe, T. Parikh, M. Schnepp et al., Optimal beam loading in a laser-plasma accelerator, Phys. Rev. Lett. 126, 174801 (2021).

[5] S. Jalas, M. Kirchen, C. Braun, T. Eichner, J. Gonzalez, L. Hübner, T. Hülsenbusch, P. Messner, G. Palmer, M. Schnepp et al., Tuning curves for a laser-plasma accelerator, Phys. Rev. Accel. Beams 26, 071302 (2023).

[6] European strategy for particle physics- accelerator R&D roadmap, edited by N. Mounet, CERN Yellow Reports: Monographs, CERN, Geneva, 2022, https://arxiv.org/abs/2201.07895.

[7] R. W. Assmann, M. K. Weikum, T. Akhter, D. Alesini, A. S. Alexandrova, M. P. Anania, N. E. Andreev, I. Andriyash, M. Artioli, A. Aschikhin et al., EuPRAXIA conceptual design report, Eur. Phys. J. Spec. Top. 229, 3675 (2020).

[8] K. Wille, The Physics of Particle Accelerators (Oxford University Press, New York, 2001), ISBN 9780198505495.

[9] K. Floettmann, Some basic features of the beam emittance, Phys. Rev. ST Accel. Beams 6, 034202 (2003).

[10] B. J. Holzer, Introduction to Transverse Beam Dynamics (CERN, Geneva, 2014).

[11] P. Nghiem, R. Assmann, A. Beck, A. Chancé, E. Chiadroni, B. Cros, M. Ferrario, A. F. Pousa, A. Giribono, L. Gizzi et al., Toward a plasma-based accelerator at high beam energy with high beam charge and high beam quality, Phys. Rev. Accel. Beams 23, 031301 (2020).

[12] M. E. Couprie, A. Loulergue, M. Labat, R. Lehe, and V. Malka, Towards a free electron laser based on laser plasma accelerators, J. Phys. B 47, 234001 (2014).

[13] T. André, I. A. Andriyash, A. Loulergue, M. Labat, E. Roussel, A. Ghaith, M. Khojoyan, C. Thaury, M. Valléau, F. Briquez et al., Control of laser plasma accelerated electrons for light sources, Nat. Commun. 9, 1334 (2018).

[14] A. Bernhard, V. Afonso Rodríguez, S. Kuschel, M. Leier, P. Peiffer, A. Sävert, M. Schwab, W. Werner, C. Widmann, A. Will et al., Progress on experiments towards LWFA-driven transverse gradient undulator-based FELs, Nucl. Instrum. Methods Phys. Res., Sect. A 909, 391 (2018).

[15] M. Rossetti Conti, A. Bacci, A. Giribono, V. Petrillo, A. Rossi, L. Serafini, and C. Vaccarezza, Electron beam transfer line design for plasma driven Free Electron Lasers, Nucl. Instrum. Methods Phys. Res., Sect. A 909, 84 (2018).

[16] A. Chancé, O. Delferrière, J. Schwindling, C. Bruni, N. Delerue, A. Specka, B. Cros, G. Maynard, B. S. Paradkar, and P. Mora, Transport line for a multi-staged laser-plasma acceleration: DACTOMUS, Nucl. Instrum. Methods Phys. Res., Sect. A 740, 158 (2014).

[17] T. Audet, F. Desforges, A. Maitrallain, S. D. Dufrénoy, M. Bougeard, G. Maynard, P. Lee, M. Hansson, B. Aurand, A. Persson et al., Electron injector for compact staged high energy accelerator, Nucl. Instrum. Methods Phys. Res., Sect. A 829, 304 (2016).

[18] A. Maitrallain, T. Audet, S. Dobosz Dufrénoy, A. Chancé, G. Maynard, P. Lee, A. Mosnier, J. Schwindling, O. Delferrière, N. Delerue et al., Transport and analysis of electron beams from a laser wakefield accelerator in the 100 MeV energy range with a dedicated magnetic line, Nucl. Instrum. Methods Phys. Res., Sect. A 908, 159 (2018).

[19] K. A. Dewhurst, B. D. Muratori, E. Brunetti, B. van der Geer, M. de Loos, H. L. Owen, S. M. Wiggins, and D. A. Jaroszynski, A beamline to control longitudinal phase space whilst transporting laser wakefield accelerated electrons to an undulator, Sci. Rep. 13, 8831 (2023).

[20] L. T. Dickson, C. I. D. Underwood, F. Filippi, R. J. Shalloo, J. B. Svensson, D. Guénot, K. Svendsen, I. Moulanier, S. D. Dufrénoy, C. D. Murphy et al., Mechanisms to control laser-plasma coupling in laser wakefield electron acceleration, Phys. Rev. Accel. Beams 25, 101301 (2022).

[21] P. Drobniak, E. Baynard, C. Bruni, K. Cassou, C. Guyot, G. Kane, S. Kazamias, V. Kubytsky, N. Lericheux, B. Lucas et al., Fast Particle-in-Cell simulations-based method for the optimisation of a laser-plasma electron injector, arXiv:2305.09264.

[22] S. A. Antipov, A. F. Pousa, I. Agapov, R. Brinkmann, A. R. Maier, S. Jalas, L. Jeppe, M. Kirchen, W. P. Leemans, A. M. de la Ossa et al., Design of a prototype laser-plasma injector for an electron synchrotron, Phys. Rev. Accel. Beams 24, 111301 (2021).

[23] S. Antipov, I. Agapov, R. Brinkmann, A. Ferran Pousa, M. Jebramcik, A. Martinez de la Ossa, and M. Thévenet, First start-to-end simulations of the 6 GeV laser-plasma injector at DESY, in Proceedings of the 13th International Particle Accelerator Conference, IPAC-2022, Bangkok, Thailand (JACoW, Geneva, Switzerland, 2022), WEPOST029, 10.18429/JACoW-IPAC2022-WEPOST029.

[24] M. Migliorati, A. Bacci, C. Benedetti, E. Chiadroni, M. Ferrario, A. Mostacci, L. Palumbo, A. R. Rossi, L. Serafini, and P. Antici, Intrinsic normalized emittance growth in laser-driven electron accelerators, Phys. Rev. ST Accel. Beams 16, 011302 (2013).

[25] K. Floettmann, Adiabatic matching section for plasma accelerated beams, Phys. Rev. ST Accel. Beams 17, 054402 (2014).

[26] X. Li, A. Chancé, and P. A. P. Nghiem, Preserving emittance by matching out and matching in plasma wakefield acceleration stage, Phys. Rev. Accel. Beams 22, 021304 (2019).

[27] E. Adli, A. Ahuja, O. Apsimon, R. Apsimon, A.-M. Bachmann, D. Barrientos, F. Batsch, J. Bauche, V. K. B. Olsen, M. Bernardin et al., Acceleration of electrons in the plasma wakefield of a proton bunch, Nature (London) 561, 363 (2018).

[28] E. Gschwendtner, K. Lotov, P. Muggli, M. Wing, R. Agnello, C. C. Ahdida, M. C. Amoedo Goncalves, Y. Andrebe, O. Apsimon, R. Apsimon et al., The AWAKE Run 2 programme and beyond, Symmetry 14, 1680 (2022).

[29] D. F. G. Minenna, C. Ballage, V. Bencini, S. Bethuys, B. Cros, L. Dickson, S. Doebert, J. Farmer, E. Gschwendtner, A. Jeandet et al., EARLI: Design of a laser wakefield accelerator for AWAKE, in Proceedings of the 14th International Particle Accelerator Conference, IPAC-

2023, Venice, Italy (JACoW, Geneva, Switzerland, 2023), 10.18429/JACoW-IPAC2023-TUPA089.

[30] J. M. Arnesano and S. Dobert, Design of an x-band bunching and accelerating system for AWAKE Run 2, in *Proceedings of the 31st International Linear Accelerator Conference, LINAC-2022, Liverpool, United Kingdom* (JACoW, Geneva, Switzerland, 2022), 10.18429/JACoW-LINAC2022-TUPOPA24.

[31] R. Ramjiawan, S. Döbert, J. Farmer, E. Gschwendtner, P. Muggli, F. Velotti, and L. Verra, Design of the proton and electron transfer lines for AWAKE Run 2c, in *Proceedings of the 12th International Particle Accelerator Conference, IPAC-2021, Campinas, SP, Brazil* (JACoW, Geneva, Switzerland, 2021), 10.18429/JACoW-IPAC2021-MOPAB241.

[32] J. M. Cole, J. C. Wood, N. C. Lopes, K. Poder, R. L. Abel, S. Alatabi, J. S. J. Bryant, A. Jin, S. Kneip, K. Mecseki *et al.*, Laser-wakefield accelerators as hard x-ray sources for 3D medical imaging of human bone, Sci. Rep. **5**, 13244 (2015).

[33] W. Wang, K. Feng, L. Ke, C. Yu, Y. Xu, R. Qi, Y. Chen, Z. Qin, Z. Zhang, M. Fang *et al.*, Free-electron lasing at 27 nanometres based on a laser wakefield accelerator, Nature (London) **595**, 516 (2021).

[34] M. Labat, J. C. Cabadağ, A. Ghaith, A. Irman, A. Berlioux, P. Berteaud, F. Blache, S. Bock, F. Bouvet, F. Briquez *et al.*, Seeded free-electron laser driven by a compact laser plasma accelerator, Nat. Photonics **17**, 150 (2022).

[35] C. DesRosiers, V. Moskvin, A. F. Bielajew, and L. Papiez, 150–250 MeV electron beams in radiation therapy, Phys. Med. Biol. **45**, 1781 (2000).

[36] M.-C. Vozenin, J. Bourhis, and M. Durante, Towards clinical translation of FLASH radiotherapy, Nat. Rev. Clin. Oncol. **19**, 791 (2022).

[37] C. B. Schroeder, E. Esarey, C. G. R. Geddes, C. Benedetti, and W. P. Leemans, Physics considerations for laser-plasma linear colliders, Phys. Rev. ST Accel. Beams **13**, 101301 (2010).

[38] C. McGuffey, A. G. R. Thomas, W. Schumaker, T. Matsuoka, V. Chvykov, F. J. Dollar, G. Kalintchenko, V. Yanovsky, A. Maksimchuk, K. Krushelnick *et al.*, Ionization induced trapping in a laser wakefield accelerator, Phys. Rev. Lett. **104**, 025004 (2010).

[39] A. Pak, K. A. Marsh, S. F. Martins, W. Lu, W. B. Mori, and C. Joshi, Injection and trapping of tunnel-ionized electrons into laser-produced wakes, Phys. Rev. Lett. **104**, 025003 (2010).

[40] M. Chen, E. Esarey, C. B. Schroeder, C. G. R. Geddes, and W. P. Leemans, Theory of ionization-induced trapping in laser-plasma accelerators, Phys. Plasmas **19**, 033101 (2012).

[41] P. Lee, G. Maynard, T. Audet, B. Cros, R. Lehe, and J.-L. Vay, Optimization of laser-plasma injector via beam loading effects using ionization-induced injection, Phys. Rev. Accel. Beams **21**, 052802 (2018).

[42] R. Lehe, M. Kirchen, I. A. Andriyash, B. B. Godfrey, and J.-L. Vay, A spectral, quasi-cylindrical and dispersion-free Particle-In-Cell algorithm, Comput. Phys. Commun. **203**, 66 (2016).

[43] M. Santarsiero, D. Aiello, R. Borghi, and S. Vicalvi, Focusing of axially symmetric flattened Gaussian beams, J. Mod. Opt. **44**, 633 (1997).

[44] T. Audet, P. Lee, G. Maynard, S. D. Dufrénoy, A. Maitrallain, M. Bougeard, P. Monot, and B. Cros, Gas cell density characterization for laser wakefield acceleration, Nucl. Instrum. Methods Phys. Res., Sect. A **909**, 383 (2018).

[45] W. Lu, M. Tzoufras, C. Joshi, F. S. Tsung, W. B. Mori, J. Vieira, R. A. Fonseca, and L. O. Silva, Generating multi-GeV electron bunches using single stage laser wakefield acceleration in a 3D nonlinear regime, Phys. Rev. ST Accel. Beams **10**, 061301 (2007).

[46] S. Jalas, M. Kirchen, P. Messner, P. Winkler, L. Hübner, J. Dirkwinkel, M. Schnepp, R. Lehe, and A. R. Maier, Bayesian optimization of a laser-plasma accelerator, Phys. Rev. Lett. **126**, 104801 (2021).

[47] X. Li, A. Mosnier, and P. A. P. Nghiem, Design of a 5 GeV laser-plasma accelerating module in the quasi-linear regime, Nucl. Instrum. Methods Phys. Res., Sect. A **909**, 49 (2018).

[48] X. Li, P. A. P. Nghiem, and A. Mosnier, Toward low energy spread in plasma accelerators in quasilinear regime, Phys. Rev. Accel. Beams **21**, 111301 (2018).

[49] M. Tzoufras, W. Lu, F. S. Tsung, C. Huang, W. B. Mori, T. Katsouleas, J. Vieira, R. A. Fonseca, and L. O. Silva, Beam loading by electrons in nonlinear plasma wakes, Phys. Plasmas **16**, 056705 (2009).

[50] D. Uriot and N. Pichoff, Status of TraceWin code, in *Proceedings of the 6th International Particle Accelerator Conference, IPAC-2015, Richmond, VA* (JACoW, Geneva, Switzerland, 2015), 10.18429/JACoW-IPAC2015-MOPWA008.

[51] F. Marteau, A. Ghaith, P. N'Gotta, C. Benabderrahmane, M. Valléau, C. Kitegi, A. Loulergue, J. Vétéran, M. Sebdaoui, T. André *et al.*, Variable high gradient permanent magnet quadrupole (QUAPEVA), Appl. Phys. Lett. **111**, 253503 (2017).

[52] J. Derouillat, A. Beck, F. Pérez, T. Vinci, M. Chiaramello, A. Grassi, M. Flé, G. Bouchard, I. Plotnikov, N. Aunai *et al.*, Smilei: A collaborative, open-source, multi-purpose particle-in-cell code for plasma simulation, Comput. Phys. Commun. **222**, 351 (2018).

[53] A. Lifschitz, X. Davoine, E. Lefebvre, J. Faure, C. Rechatin, and V. Malka, Particle-in-Cell modelling of laser–plasma interaction using Fourier decomposition, J. Comput. Phys. **228**, 1803 (2009).

[54] J.-L. Vay, Noninvariance of space- and time-scale ranges under a lorentz transformation and the implications for the study of relativistic interactions, Phys. Rev. Lett. **98**, 130405 (2007).

[55] M. Chen, E. Cormier-Michel, C. Geddes, D. Bruhwiler, L. Yu, E. Esarey, C. Schroeder, and W. Leemans, Numerical modeling of laser tunneling ionization in explicit particle-in-cell codes, J. Comput. Phys. **236**, 220 (2013).

[56] F. Massimo, I. Zemzemi, A. Beck, J. Derouillat, and A. Specka, Efficient cylindrical envelope modeling for laser wakefield acceleration, J. Phys. Conf. Ser. **1596**, 012055 (2020).

[57] D. Terzani and P. Londrillo, A fast and accurate numerical implementation of the envelope model for laser–plasma dynamics, Comput. Phys. Commun. **242**, 49 (2019).

[58] F. Massimo, A. Beck, J. Derouillat, M. Grech, M. Lobet, F. Pérez, I. Zemzemi, and A. Specka, Efficient start-to-end 3D envelope modeling for two-stage laser wakefield acceleration experiments, Plasma Phys. Controlled Fusion **61**, 124001 (2019).

[59] F. Massimo, A. Beck, J. Derouillat, I. Zemzemi, and A. Specka, Numerical modeling of laser tunneling ionization in particle-in-cell codes with a laser envelope model, Phys. Rev. E **102**, 033204 (2020).

[60] P.-L. Bourgeois and X. Davoine, Improved modellisation of laser–particle interaction in particle-in-cell simulations, J. Plasma Phys. **89**, 905890206 (2023).